Effect of ultrasonic power on microstructure and properties of ultrasonic electrodeposited $ZnCo_2O_4$ anode nanomaterials

Dong Liu [a,b,c,*], Hailong Fu [b,c], Xu Zhu [a], Longqing Zou [b,c]

[a] School of Mechanical and Electronic Engineering, Qiqihar University, Qiqihar 161006, China
[b] Research Institute of Applied Technology, Northeast Petroleum University, Daqing 163318, China
[c] School of Mechanical Science and Engineering, Northeast Petroleum University, Daqing 163318, China

ARTICLE INFO

ABSTRACT

Ultrasonic electrodeposition was employed to manufacture $ZnCo_2O_4$ anode nanomaterials (ZCOAN), with the objective of utilization as high-performance anode materials for lithium-ion batteries. The influence of ultrasonic power on various characteristics of ZCOAN, including surface morphology, phase composition, crystal structure, and electrochemical properties was also investigated. The results indicated that $ZnCo_2O_4$ anode nanomaterials prepared at 600 W demonstrated a spinel surface structure with polyporous dendrite spores and a subcrystalline size of 11.68 nm. Moreover, the prepared ZCOAN material demonstrated polyporous morphological characteristics and well-organized particles. Diffraction peaks were identified at specified angles in all ZCOAN samples: $31.26°$, $36.93°$, $46.38°$, $54.13°$, $59.87°$, and $66.17°$ corresponding to the crystallographic planes (200), (311), (400), (422), (511), and (440), respectively. The appearance of these peaks confirms the presence of a spinel structure in the ZCOAN samples. A smaller grain size results in increased gaps and a larger surface area, thereby promoting ion exchange. Therefore, $ZnCo_2O_4$ anode nanomaterials synthesized at 600 W showed superior electrochemical performance compared to other samples. They demonstrated the highest charge capacity ($\sim$1176 mAh·g^{-1}), discharge capacity ($\sim$1160 mAh·g^{-1}), and stability, along with a minimal electrical impedance (35.65 Ω) at a constant current density of 150 mA·g^{-1}. Furthermore, the coulomb efficiency of this nanomaterial remained high at 98.6 % after 1200 cycles, indicating its excellent cycling performance.

1. Introduction

As an advanced form of green energy technology, lithium-ion batteries have undergone significant advancements, and are now extensively used in a variety of industries, including agricultural machinery, energy storage, electric vehicles, and aerospace (Ogumi, 2010; Zhou et al., 2021; Tarascon and Armand, 2021; Goodenough and Park, 2013; Etacheri et al., 2011). However, due to scientific and technological advancements and rising energy demands, the conventional graphite electrode materials used in lithium-ion batteries fall short of meeting the demands for high energy density (Wu and Xiao, 2021; Xu et al., 2019; Qin et al., 2017; Yan et al., 2020). Graphite electrode material has been commonly utilized as an anode material in traditional industries. However, its theoretical mass-specific capacity is only 372 mAh·g^{-1}, severely limiting the specific capacity, charge–discharge ratio, and other electrochemical properties of batteries employing a graphite anode (Li and Maier, 2010; Winter and Brodd, 2004; Wang et al., 2020; Wang et al., 2019). There is, therefore, a growing research interest in developing new anode materials that possess high specific energy, excellent reversibility of charge and discharge reactions, and outstanding cost-effectiveness.

Currently, cobalt oxide (Co_3O_4) stands out due to its advantageous combination of a high specific capacity, a relatively small specific surface area, and satisfactory charge–discharge cycle performance (Mahmood et al., 2018; Wang et al., 2019; Wang et al., 2018). This set of characteristics has propelled Co_3O_4 to widespread popularity as a preferred anode material in various applications (Qi et al., 2020). However, the cobalt-containing oxide is toxic and inefficient and is unlikely to be used as a direct alternative to graphite as an ideal anode material. In comparison, $ZnCo_2O_4$ anode nanomaterials (ZCOAN) as electrode materials for lithium-ion batteries demonstrate advantages such as high capacity, excellent cyclic stability, and abundant availability of resources. ZCOAN also exhibits a notable safety advantage, a characteristic that has drawn attention from researchers both
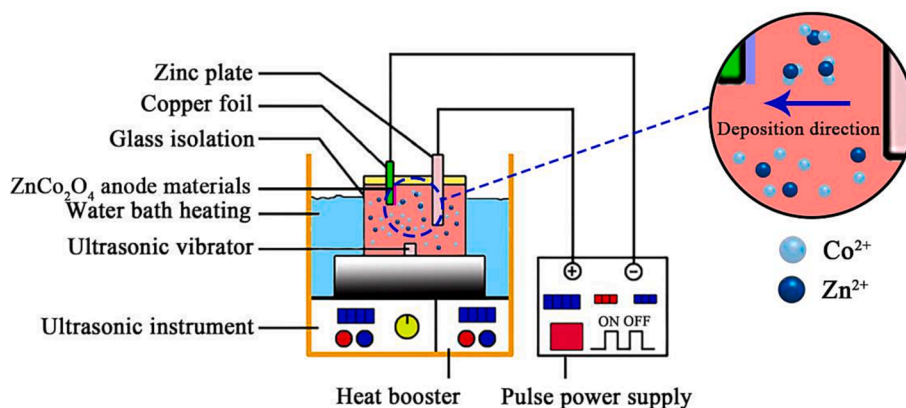
Fig. 1. Experimental setup for fabricating $ZnCo_2O_4$ anode nanomaterials.

Table 1
Electrolyte composition for fabricating $ZnCo_2O_4$ anode nanomaterials.

Chemical reagents	Parameters
$Co(NO_3)_2 \cdot 6H_2O$ (g·L^{-1})	30
$Zn(NO_3)_2 \cdot 6(H_2O)$ (g·L^{-1})	60
CH_4N_2O (g·L^{-1})	72
H_3BO_3 (g·L^{-1})	30
$C_{12}H_{25}SO_4Na$ (g·L^{-1})	0.1
$C_7H_4NNaO_3S$ (g·L^{-1})	0.15

Table 2
Experimental conditions for the synthesis of $ZnCo_2O_4$ anode nanomaterials.

Items	Parameters
Plating bath temperature (°C)	60
Plating current density (A·dm^{-2})	4
Stirring rate (r·min^{-1})	1000
Ultrasonic power (W)	200–800
Activation time (min)	10
pH	4.2
Pulse frequency (Hz)	500

Table 3
Effect of ultrasonic power on the grains diameter of $ZnCo_2O_4$ composites.

Ultrasonic power (W)	Diameter of nickel grain (nm)			
	(1 1 1)	(2 0 0)	(2 2 0)	Average size
200	18.64	13.82	9.99	14.15
400	17.28	11.93	8.98	12.73
600	15.13	8.41	5.14	9.56
800	16.97	10.15	7.92	11.68

domestically and internationally (Sun et al., 2019; Yu et al., 2017). Currently, the predominant techniques employed for the synthesis of $ZnCo_2O_4$ anode nanomaterials (ZCOAN) include hydrothermal synthesis, high-temperature calcination, and chemical vapor precipitation. Wang *et al.* (Wang et al., 2016) used a simple hydrothermal approach to produce nanorods on reduced graphene oxide (rGO) nanosheets. The developed $ZnCo_2O_4$/rGO electrode demonstrated enhanced electrochemical performance with a significant specific capacitance of 626F/cm^2 when evaluated at 1 A·g^{-1}. Furthermore, it manifested an excellent rate capability, retaining 81 % of its initial capacitance at 30 A·g^{-1}. The electrode also exhibited long-term cycling stability, enduring 3000 cycles when subjected to an electric current density of 10 A·g^{-1}. Lu *et al.* (Lu et al., 2016) carried out the preparation of $Zn_{0.33}Co_{0.67}CO_3$ (ZCCO) microspheres by solvothermal method at different temperatures. The results show that ZCCO obtained by pyrolysis at 200 °C has a high discharge capacity of 1416 mAh/g and a good cyclic stability of 741 mAh/g.

Compared to the previously mentioned preparation methods, ultrasonic electrodeposition technology offers significant advantages, including increased deposition efficiency, improved surface quality of materials, enhanced adhesion, controlled microstructure, and energy-saving benefits. However, there is a limited number of scientific reports on $ZnCo_2O_4$ anode nanomaterial (ZCOAN) electrodes fabricated using the ultrasonic electrodeposition method. Therefore, this study employed the ultrasonic electrodeposition technique for synthesizing ZCOAN. Various techniques, such as scanning electron microscopy (SEM), X-ray diffractometry (XRD), X-ray photoelectron spectroscopy (XPS), and electrochemical analysis, were utilized to examine the surface microstructure, phase composition, and crystal structure of the synthesized ZCOAN. Additionally, the electrochemical performance of the battery assembled with ZCOAN was investigated using cyclic voltammetry (CV), constant current charge and discharge (CCD), and electrochemical impedance spectroscopy (EIS).
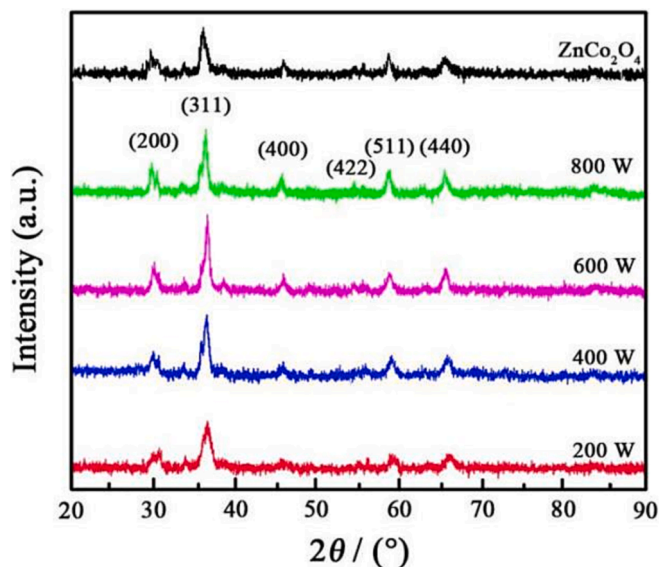

Fig. 2. XRD patterns of $ZnCo_2O_4$ fabricated with varying ultrasonic powers.
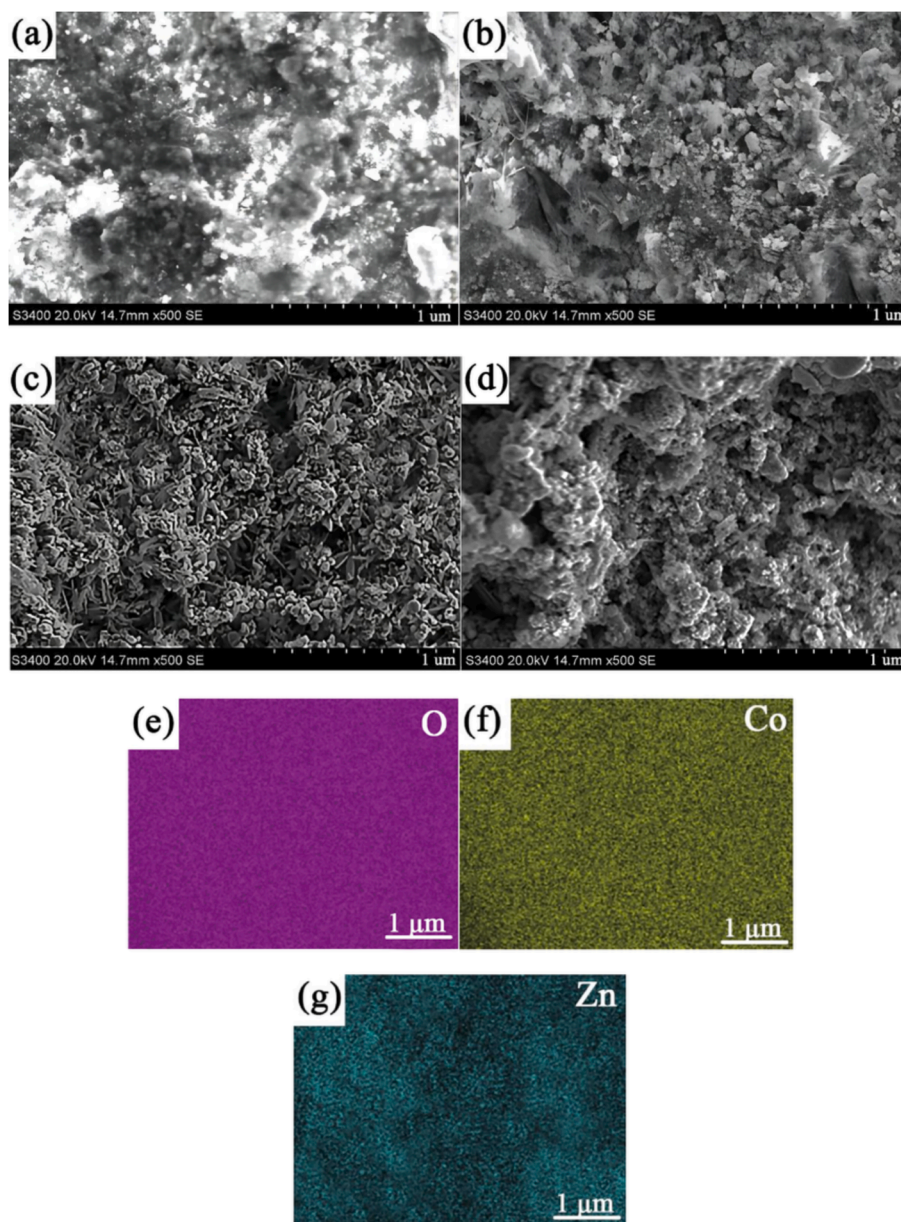
Fig. 3. SEM images of $ZnCo_2O_4$ fabricated at different ultrasonic powers: (a) 200 W, (b) 400 W, (c) 600 W, (d) 800 W, (e-g) energy dispersive X-ray EDX distribution of O, Co and Zn elements in the range of SEM images and (h) EDS elemental mapping of $ZnCo_2O_4$ at ultrasonic power 600 W.

2. Experimental section

2.1. Preparation

During the ultrasonic electrodeposition process, the anode material was based on a zinc plate (purity $\geq$ 99.9 %), and copper foil (5 cm $\times$ 5 cm) was used as anode material. The cathode and anode were separated by 35 mm. Fig. 1 illustrates the scheme of an ultrasonic electrodeposition experiment used for the synthesis of $ZnCo_2O_4$ anode nanomaterial. Before the experiment, the surface of the sample was cleaned with ultrasonic waves for 30 min, washed with anhydrous ethanol and deionized water, and then dried in a vacuum drying chamber for 10 h. The reagent used in the plating solution was of analytical purity. Table 1 provides the compositions of the electrolytes. During the electrodeposition procedure, the electroplating power was supplied by a WYJ-3010-type power supply. A KQ-300VDB type three-frequency numerical control ultrasonic cleaner ultrasonic generator was used to prevent the

agglomeration of $ZnCo_2O_4$ anode nanomaterial. An EMS-12 underwater remote control stirrer was employed for magnetic stirring. The experimental conditions for the synthesis of $ZnCo_2O_4$ anode nanomaterial have been presented in Table 2.

The CR-2032 lithium-ion button battery was evaluated for its electrochemical performance. CR-2032 button battery was selected because of its compact and convenient, voltage stability and long service life. The anode nanomaterial was composed of 0.42 g $ZnCo_2O_4$ acquired through electro-sedimentary cathode material, constituting 70 wt% of the sample. Additionally, 0.12 g of Super P conductive material, representing 20 wt% of the conductive agent, and 0.06 g of a binder mixture consisting of carboxymethyl cellulose and styrene-butadiene rubber in a 1:1 ratio, accounting for 10 wt%, were included. Carboxymethyl cellulose and styrene-butadiene rubber had minimal impact on charge–discharge performance due to their modest concentration. These components underwent thorough mixing and stirring before being uniformly coated onto a copper foil. Battery pole pieces with a 6 mm radius were
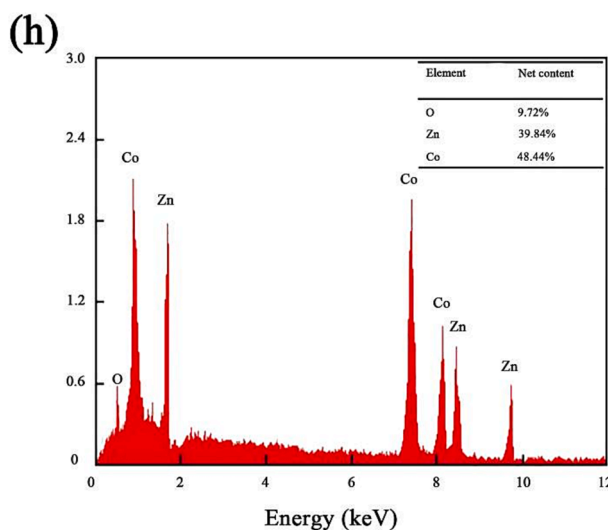
Element	Net content
O	9.72%
Zn	39.84%
Co	48.44%

Fig. 3. (*continued*).

subsequently cut from the resulting material. The electrolyte composition in the lithium-ion battery comprised lithium salt, LiPF$_6$, at a concentration of 1 mol·L^{-1}. A combination of propylene carbonate (PC), a cyclic carbonate, and diethyl carbonate (DEC), a straight chain carbonate, in a volume ratio of 1:1 (V(PC):V(DEC)) was employed as a solvent. The diaphragm material employed in the battery was Celgard 2300. The CR 2032 lithium-ion button battery was assembled using vacuum gloves and sealed in an argon-controlled atmosphere.

2.2. Characterization

The phase composition and crystal structure of the sample were determined by XRD (Rigaku, D/max-2400). XRD was used to acquire and analyze the diffraction pattern of the material. The phase structural analysis of the ZnCo$_2$O$_4$ anode nanomaterial was carried out through an X-ray diffraction meter. The particle size of ZnCo$_2$O$_4$ anode nanomaterial was determined using Scherrer's formula, as presented in Eq. (1) (Baranova et al., 2009). The following are the operational parameters: CuKα was used as a transmitting source; the tube voltage and tube current were set at 30 kV; Bragg coupling mode was utilized as scanning mode with the scanning step equivalent to 0.5°, while the scanning rate was maintained at 4°/min.

The ZnCo$_2$O$_4$ anode nanomaterials served as the negative electrode in the lithium-ion battery, while a lithium sheet was employed as the positive electrode. A lithium-ion button battery was constructed from these parts. A CHI660C-style electrochemical workstation (Shanghai Chenhua Instrument Co., LTD) was used to perform the CV and EIS analysis of a lithium-ion button battery. The operation parameters included a working voltage window of 0.01 ~ 3.00 V (vs. Li/Li$^+$), a scanning speed of 0.4 mV·s^{-1}, a scanning frequency of 0.01 Hz ~ 100 kHz, and a vibration amplitude of 4 mV. The lithium-ion button battery was subjected to a constant current charge and discharge examination using the CT2001A Land Battery Test System (Wuhan Barrui Technology Co., LTD).

3. Result and discussion

3.1. XRD analysis

Fig. 2 shows the XRD pattern of ZnCo$_2$O$_4$ synthesized using varying ultrasonic powers. With the increase of ultrasonic power from 200 W to 600 W, the diffraction peak intensity of ZnCo$_2$O$_4$ underwent a gradual increase. However, with the increase in ultrasonic power to 800 W, a decrease in diffraction peak intensity was observed. The grain sizes of ZnCo$_2$O$_4$ obtained at 200 W, 400 W, 600 W, and 800 W were found to be 14.15 nm, 12.73 nm, 9.56 nm, and 11.68 nm, respectively. The detailed lattice parameters of ZCOAN have been displayed in Table 3. The observed outcomes can be attributed to the utilization of ultrasonic technology, which introduced a sufficient number of nucleation sites, leading to grain refinement. Simultaneously, the application of ultrasonic waves to the electrolyte generated a microvortex effect, thereby reducing concentration polarization and enhancing the deposition rate. However, the application of 800 W of ultrasonic power led to the occurrence of microwave vibrations within the electrolyte, hindering the formation and proliferation of grains. Furthermore, Distinct diffraction peaks were observed at specific angles in all ZCOAN anode nanomaterials: 31.26°, 36.93°, 46.38°, 54.13°, 59.87°, and 66.17°, which respectively correspond to the (200), (311), (400), (422), (511), and (440) crystallographic planes. However, the diffraction peaks at 31.26° and 36.93° showed splitting due to the formation of hexagonal close-packed (HCP/Wurtzite) ZnO during electrodeposition. The Zn phase plays a key role in ZnCo$_2$O$_4$ materials, which can improve the stability of the electrode structure, improve the conductivity and increase the active site. Comparison of the diffraction peaks of samples with a standard comparison card (JCPDS card No. 23–1390) demonstrated that ZnCo$_2$O$_4$ possessed a spinel structure. The results of XRD for ZnCo$_2$O$_4$ anode nanomaterial were in agreement with the previously reported studies (Liu and Hu, 2018; Liu et al., 2015).

3.2. SEM observation

Fig. 3(a-d) displays SEM images of ZnCo$_2$O$_4$ fabricated at different ultrasonic powers. Additionally, Fig. 3(e-g) presents the EDX energy spectrum of ZnCo$_2$O$_4$ prepared using an ultrasonic power of 600 W. The abundance of the oxygen (O) element is the highest, while the abundance of the cobalt (Co) element is higher than that of the zinc (Zn) element, aligning with the expected chemical composition of the material. Fig. 3(h) illustrates the EDS element mapping diagram, indicating the specific content of each element. At an ultrasonic power of 200 W, it was observed that the agglomeration of ZnCo$_2$O$_4$ anode nanomaterials was insufficient, providing an inadequate number of binding sites for the insertion and detachment of lithium ions. This unfavorable condition hinders the efficient transport and delivery of lithium ions. As the ultrasonic power increased, the ordered arrangement and the large gaps within the ZnCo$_2$O$_4$ anode nanomaterials also increased. At the 400 W ultrasonic power level, a limited presence of dendrite structures was noted on the surface, and the phenomenon of particle agglomeration persisted. Notably, at an ultrasonic power of 600 W, the ZnCo$_2$O$_4$ anode
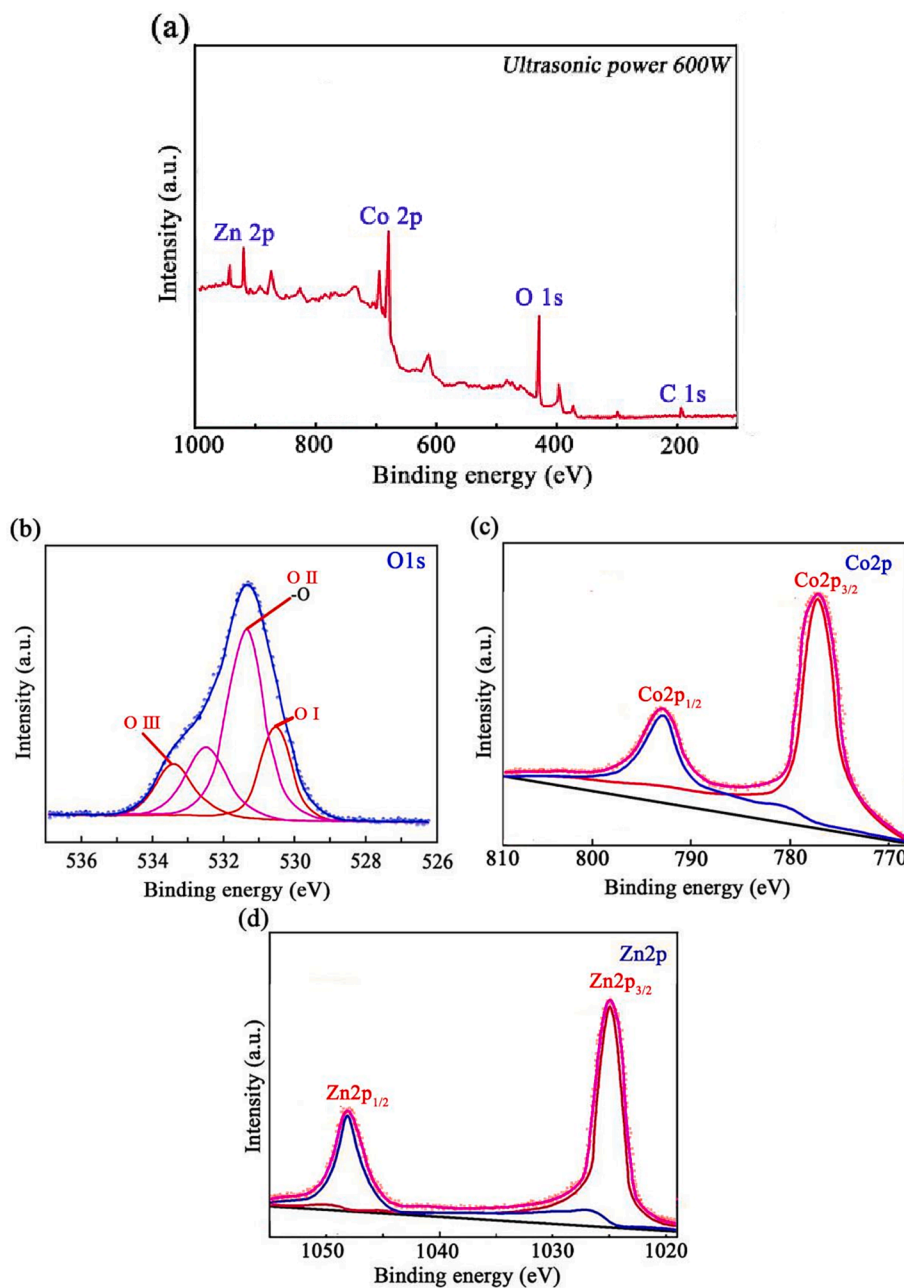
Fig. 4. XPS spectrum of $ZnCo_2O_4$ anode nanomaterials: (a) XPS overall figure, (b) O1s, (c) Co2p, and (d) Zn2p.

nanomaterial displayed a more compact and dendritic morphology. The compact structure and voids existing within $ZnCo_2O_4$ anode nanomaterial were employed as an advantageous pathway for the insertion and removal of lithium ions in the electrolyte. This facilitated the reduction of volume fluctuations in the cathode material during the charge and discharge cycles. The phenomenon of agglomeration and the voids within $ZnCo_2O_4$ anode nanomaterial underwent an increase when subjected to ultrasonic power of 800 W. This phenomenon can be ascribed to the large ultrasonic power, inducing an increased intermolecular distance and consequently leading to a disorderly and displaced deposition phenomenon. Therefore, optimal ultrasonic power proves advantageous in enhancing the surface morphology and crystal size of $ZnCo_2O_4$ anode nanomaterial.

3.3. XPS analysis

Fig. 4(a-d) shows the XPS spectra of $ZnCo_2O_4$ anode nanomaterial

fabricated using an ultrasonic power of 600 W. Fig. 4a illustrates the prominent peaks associated with the elements oxygen, cobalt, and zinc. The weak peak observed at the C1s binding energy of 284.8 eV can be attributed to a carbon-containing impurity present in the substance. This peak serves as a standard for charge calibration in XPS analysis (Yi et al., 2020). The characteristic peaks of O1s are shown in Fig. 4b, which were fitted using Gaussian fitting (Wei et al., 2022). The O1s spectrum shows distinct peaks at 530.4 eV, 531.3 eV, and 533.6 eV. The O (I) peak signifies oxygen atoms bonded with Co^{2+} and Zn^{2+} ions, demonstrating a robust interaction with the metal ions and consequently yielding a lower binding energy. The O (II) peak represents oxygen atoms in water molecules, which, due to a comparatively looser bond than O (I) oxygen atoms, exhibit a slightly higher binding energy. The O (III) peak corresponds to oxygen atoms adsorbed on the sample surface, characterized by weaker interactions with the substrate and existing in a free state, hence displaying the highest binding energy. Fig. 4c exhibits the Co2p spectrum, characterized by the presence of two spin–orbit splitting
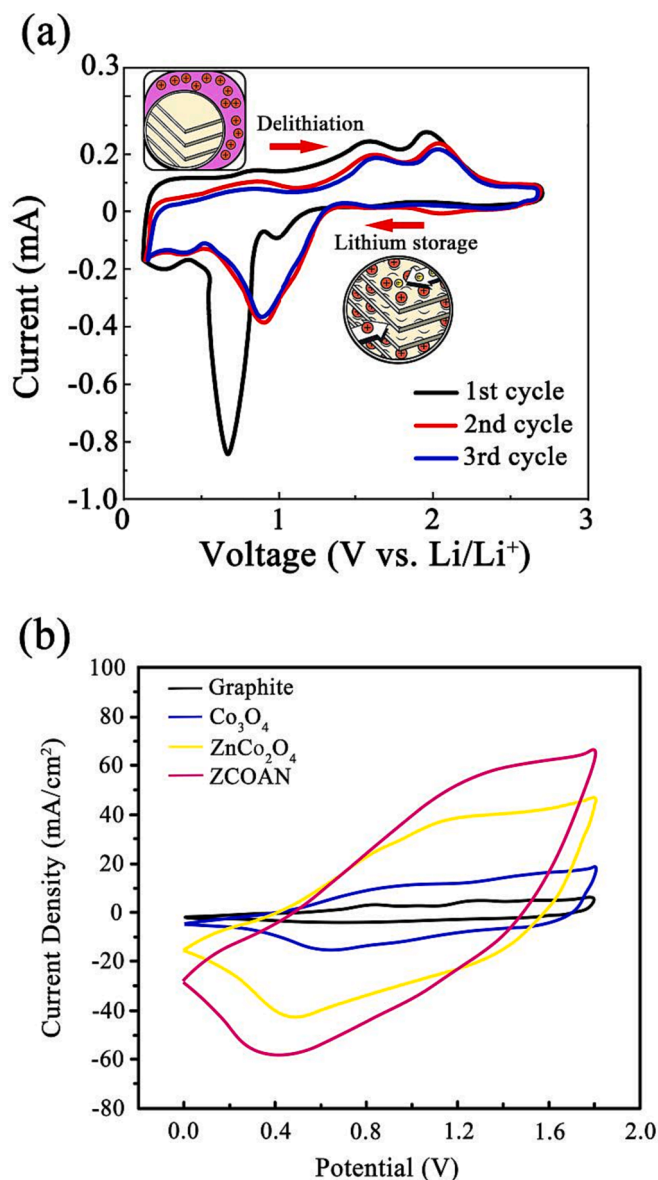
According to Fig. 4d, two peaks at 1021.1 eV and 1042.9 eV correspond to $Zn2p_{3/2}$ and $Zn2p_{1/2}$, respectively. In $ZnCo_2O_4$ anode nanomaterial, the atomic content ratio of Zn:Co was calculated to be 1:2.12, which is close to the theoretical value of 1:2. The difference observed can potentially be attributed to the presence of the positively charged metallic Zn^{2+} ions during the electrodeposition procedure (Liu et al., 2023).

3.4. Cyclic voltammetry test

The $ZnCo_2O_4$ anode nanomaterials were synthesized using an ultrasonic power of 600 W, and subsequently combined with lithium sheets to construct lithium-ion batteries. The electrochemical performance of these batteries was evaluated using an electrochemical workstation. The CV curves of $ZnCo_2O_4$ anode nanomaterials have been depicted in Fig. 5(a). In contrast to the CV curves observed in the second and third cycles, the CV curve obtained during the first cycle at a potential of 0.68 V displayed a notable difference, marked by the presence of a sharp reduction peak. This outcome can be attributed to the occurrence of a REDOX reaction on the surface of the electrode, resulting in the formation of a passivation film with a thickness ranging from 100 to 120 nm during the first charge–discharge cycle of the lithium-ion battery. The passivation film's microstructure is commonly referred to as the solid electrolyte interface (SEI). Furthermore, the CV curves of ZCOAN were compared with those of common anode materials, and the results are depicted in Fig. 5(b). The area enclosed by the cyclic voltammetry curve of ZCOAN is the largest, signifying that the REDOX reaction of ZCOAN material is the most prominent. A substantial CV

Fig. 5. Cyclic voltammetry test of ZCOZN and different anode materials (a) Cyclic voltammetry curves of ZCOAN and (b) Cyclic voltammetry curves of different anode materials.

peaks and two adjacent satellite peaks. The binding energies corresponding to the peaks observed at 778.2 eV and 795.3 eV were respectively attributed to Co^{3+} and Co^{2+} ions. Considering the coexistence of Co^{2+} and Co^{3+} in specific ratios within the sample, it can be deduced that the cobalt oxide present is Co_3O_4 (Wei et al., 2023).
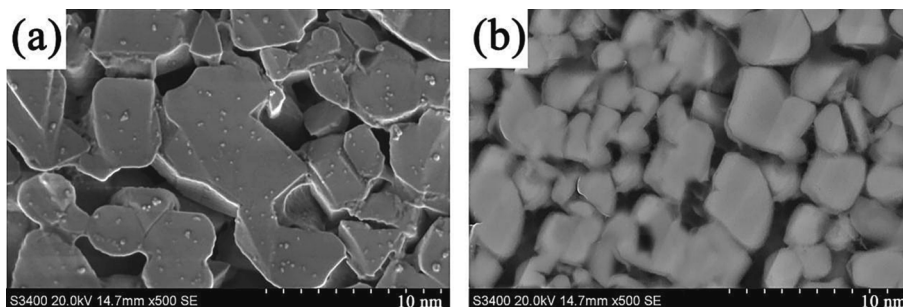

Fig. 7. Functional mechanism diagram of SEI membrane.

Fig. 6. Surface morphologies of SEI membrane following (a) the initial and (b) the 1200th charging cycles.
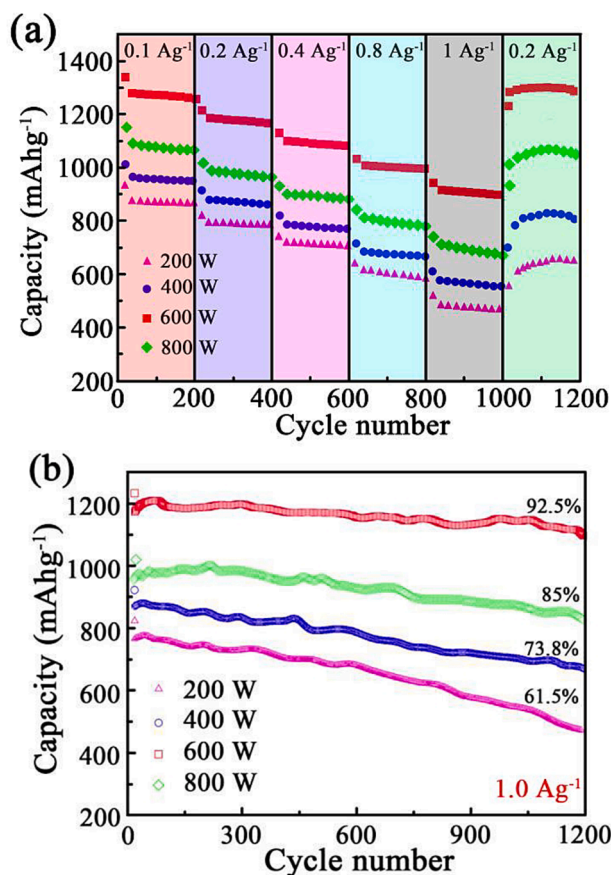
Fig. 8. Electrochemical property of ZnCo$_2$O$_4$ anode nanomaterials: (a) charge–discharge ratio, and (b) charge–discharge stability property.

curve area also indicates a high energy storage capacity and good charge transfer efficiency, both of which are pivotal for enhancing battery performance. Fig. 6 displays the surface morphologies of the SEI membrane following the initial and the 1200th charging cycles. Fig. 6(a) displays the initial surface morphology of the SEI membrane formed during the first charge–discharge cycle, while Fig. 6(b) represents the surface morphology following 1200 charge cycles. The SEI membrane was found to be in organic solvents and demonstrated stable chemical performance, thereby enhancing the electrode's cycle stability and prolonging its service life. Fig. 7 presents the functional mechanism of the SEI membrane. The SEI membrane functions as a solid electrolyte on the negative electrode, allowing for the unrestricted insertion and detachment of Li$^+$ ions. Moreover, the Solid Electrolyte Interphase (SEI) membrane acted as a barrier, preventing the co-embedding of electrolyte molecules and thereby preventing irreversible damage to the electrode. During the embedding and detaching of Li$^+$, distinctive electrochemical features were observed, with a reduction peak and two intense oxidation peaks appearing at potentials of 0.81 V, 1.65 V, and 2.05 V, respectively. The presence of a prominent oxidation peak can be ascribed to the oxidation reaction of Zn and Co with LiO$_2$, which leads to the formation of ZnO, CoO, and Co$_3$O$_4$, as indicated in Eqs. (1–4) (Zhao et al., 2019). The aforementioned findings therefore indicated that the ZnCo$_2$O$_4$ anode nanomaterial demonstrates favorable charge–discharge reversibility and stable cycling performance.
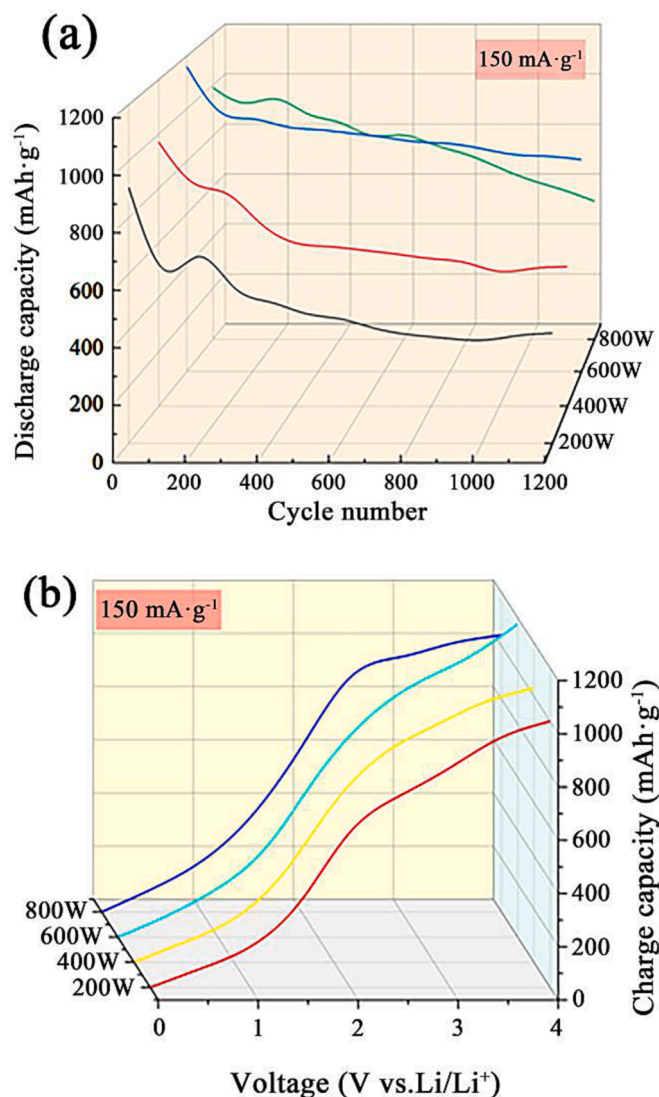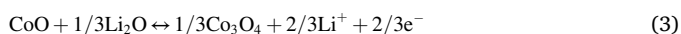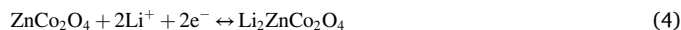
$$Zn + Li_2O \leftrightarrow ZnO + 2Li^+ + 2e^- \tag{1}$$

$$Co + Li_2O \leftrightarrow CoO + 2Li^+ + 2e^- \tag{2}$$

$$CoO + 1/3Li_2O \leftrightarrow 1/3Co_3O_4 + 2/3Li^+ + 2/3e^- \tag{3}$$

Fig. 9. Constant current charge–discharge curves of ZnCo$_2$O$_4$ at 150 mA·g^{-1}: (a) discharge curves, and (b) charge curves.

$$ZnCo_2O_4 + 2Li^+ + 2e^- \leftrightarrow Li_2ZnCo_2O_4 \tag{4}$$

3.5. Constant current charge–discharge test

Fig. 8(a) indicates the rate capability of four ZnCo$_2$O$_4$ anode nanomaterial samples with ampere density. The capacity of ZnCo$_2$O$_4$ anode nanomaterials with 600 W was superior to that of other samples, which demonstrated average charge capacities of 1247 mAhg^{-1}, 1189 mAhg^{-1}, 1106 mAhg^{-1}, 1021 mAhg^{-1}, and 929 mAhg^{-1} from 0.1 Ag^{-1} to 2 Ag^{-1}, respectively. Based on the findings, the capacity retention rate was determined to be 74.5 %. Furthermore, the rate of capacity decline in other samples was found to be higher than that of the ZnCo$_2$O$_4$ anode nanomaterial samples with a power output of 600 W. Specifically, the capacity of these samples decreased from 1150 mAhg^{-1} to 716 mAhg^{-1}, from 987 mAhg^{-1} to 607 mAhg^{-1}, and from 848 mAhg^{-1} to 497 mAhg^{-1}. Hence, the observed capacity retention rates were 62.2 %, 61.4 %, and 58.6 % respectively. After undergoing multiple charge–discharge cycles, the samples showed a decline in their capacity primarily attributed to factors such as the deactivation of active materials, alterations in the solid–liquid interface, electrolyte degradation, and internal loss or damage. These issues result in structural degradation of active materials, changes in electrolyte properties, and an elevation in
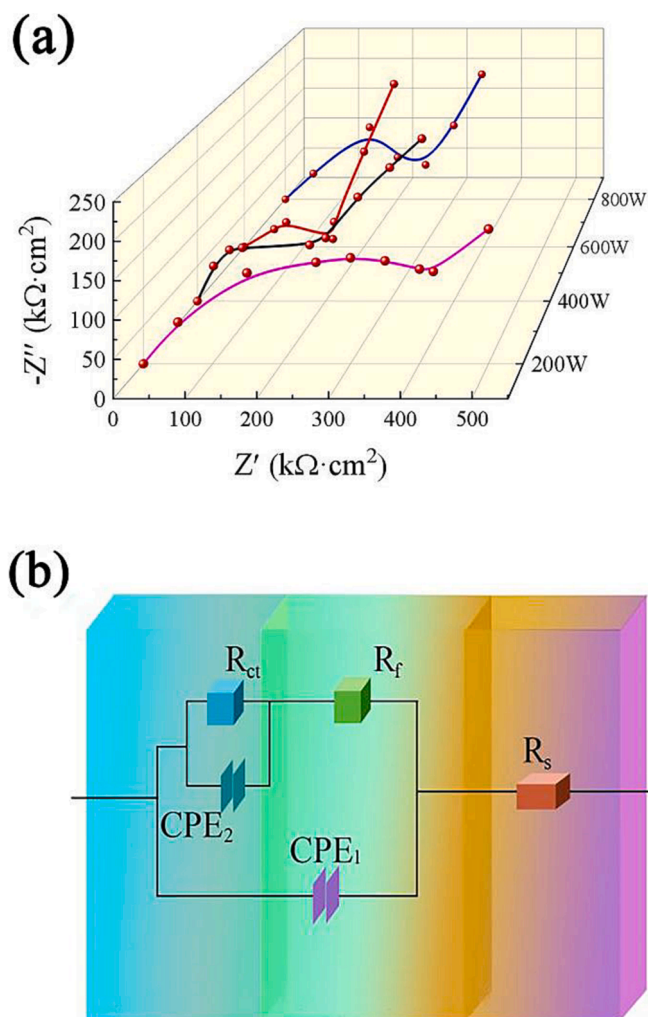
Fig. 10. Electrochemical impedance curves of $ZnCo_2O_4$ anode nanomaterials fabricated at different ultrasonic powers: (a) electrical impedance curve, and (b) equivalent circuit diagram.

Table 4

The values of resistance parameters of ZCOAN material under different ultrasonic power in EIS.

Resistance	200 W	400 W	600 W	800 W
Series resistance (Ω)transfer resistance	0.82	0.61	0.35	0.23
(Ω)	8.37	4.41	3.21	1.36
Warburg diffusion resistance (Ω)	3.85	1.32	1.19	0.99

internal resistance, collectively diminishing the effective capacity of the samples. Fig. 8(b) shows the charge–discharge stability of $ZnCo_2O_4$ anode nanomaterial at 1.0 Ag^{-1} during the 1200 cycle. Based on the outcome of the investigation, the sample prepared with 600 W of ultrasonic power exhibited the greatest cyclic stability. After 1200 charge and discharge cycles at 600 W, the capacity of $ZnCo_2O_4$ anode nanomaterial samples was well maintained, decreasing from 1189 $mAhg^{-1}$ to 1100 $mAhg^{-1}$ with a capacity retention rate of 92.5 %. Moreover, the capacity retention rates of other samples were 85.0 %, 73.8.%, and 61.5 %, respectively. To conduct a comprehensive investigation of samples for coulombic efficiency (CE), a range of current density values, ranging from 0.1 Ag^{-1} to 2 Ag^{-1}, were selected. The specific current density value chosen for testing purposes was 1.0 Ag^{-1}. Notably, the capacity initially decreases over the first 50 cycles and then progressively increases in later cycles. This phenomenon is attributed to the exposure of

Table 5

Comparison of Specific capacity of $ZnCo_2O_4$ nanomaterials prepared by ultrasonic electrodeposition with other $ZnCo_2O_4$ materials.

Material	Preparation method	Specific capacity	Cycle
$ZnCo_2O_4$@C	facile mediated solvothermal method	760.3	100
Tailored Porous $ZnCo_2O_4$	selective etching	1000	226
$Zn_{0.95}Co_2O_4$	liquid-phase co-precipitation and alkaline-tailored	652.2	200
Layer structured graphene/ porous $ZnCo_2O_4$	heat treatment	874	1000
$ZnCo_2O_4$(zinc acetate dehydrate, cobalt (II) acetate tetrahydrate, and citric acid)	rheological phase reaction	801	100
$ZnCo_2O_4$/PPy	Reflux method and chemical polymerization method	458	100
$ZnCo_2O_4$(Clew-like microshperes)	heat treatment	965	200
$ZnCo_2O_4$ nanomaterials	Ultrasonic electrodeposition	1160	1200

the electrode material to active sites during cycling, enhancing the lithium ions' intercalation/deintercalation capacity, thereby increasing the overall capacity. Moreover, although the formation of the Solid Electrolyte Interface (SEI) layer may initially impede ion transport, its subsequent stabilization and increased ion permeability over time contribute to the enhancement of battery performance (Yi et al., 2021).

Fig. 9(a) indicates the constant current discharge curves of $ZnCo_2O_4$ anode nanomaterial prepared under different ultrasonic powers at a current density of 150 mAg^{-1}. During the first cycle, the specific discharge capacity of $ZnCo_2O_4$ anode nanomaterials produced at ultrasonic powers of 200 W, 400 W, 600 W, and 800 W was 907 $mAh·g^{-1}$ and 970 $mAh·g^{-1}$, 1160 $mAh·g^{-1}$ and 990 $mAh·g^{-1}$, respectively. It is evident the one prepared at ultrasonic power of 600 W exhibited the maximum constant current specific charging capacity of 1176 $mAh·g^{-1}$, as shown in Fig. 9(b). The calculated CE value was determined to be 98.6 %. Comparably, the CE values were observed to be 90.7 %, 94.1 %, and 95.2 % for the $ZnCo_2O_4$ anode nanomaterial prepared under ultrasonic powers of 200 W, 400 W, and 800 W. The observed decrease in CE value can be attributed to the presence of a large gap between particles in the $ZnCo_2O_4$ anode nanomaterial prepared using high ultrasonic power. This gap facilitates the shedding of particles from the electrode surface, leading to a decrease in specific charging capacity. Another contributing factor to this phenomenon can be attributed to the formation of Solid Electrolyte Interphase (SEI) membranes. This observation aligns with findings reported in previous studies (Wang et al., 2017; Ru et al., 2016).

3.6. Electrochemical impedance measurement

The electrochemical impedance testing technique is commonly referred to as frequency domain impedance analysis. The electrochemical impedance curve was generated using small alternating current (AC) excitation signals, adhering to the sinusoidal law. This approach was employed to investigate the change in AC impedance with frequency under the equilibrium state of the electrochemical cell or the fixed direct current polarization condition (Shimizu et al., 2021; Fu et al., 2015). Fig. 10(a) shows the electrochemical impedance curves of $ZnCo_2O_4$ fabricated under different ultrasonic powers. Fig. 10(b) shows the corresponding equivalent circuit diagram (Shih and Liu, 2017; Liu et al., 2019; Wong et al., 2017). The electrochemical impedance curve consisted of a semi-arc at high frequencies and an oblique line at low frequencies. The impedance value of solid diffusion of lithium ions in $ZnCo_2O_4$ anode nanomaterials is represented by the low-frequency oblique line. A large slope of this line indicates a small impedance

value. The semi-arc observed in the high-frequency capacitive reactance represents the ohmic resistance and charge transfer resistance arising from the diffusion process of lithium ions within the electrolyte and the surface membrane of the $ZnCo_2O_4$ anode nanomaterial electrode. The small radius of the reactance semi-arc illustrates the low corresponding resistance (Sahoo et al., 2015; Tiwari et al., 2021). The $ZnCo_2O_4$ anode nanomaterial prepared with 600 W of ultrasonic power had the smallest impedance curve and the steepest straight-line slope, resulting in the lowest electrical impedance value. The specific values are shown in Table 4. The $ZnCo_2O_4$ anode nanomaterial synthesized at 600 W exhibited favorable reaction kinetics, as demonstrated by its relatively low ohm resistance and charge transfer resistance during the charging and discharging processes of lithium ions. Additionally, it was noted that the electrical impedance of $ZnCo_2O_4$ anode nanomaterial gradually decreased with the increase in ultrasonic power from 200 W to 600 W. However, the electrical impedance value of the $ZnCo_2O_4$ anode fabricated at 800 W was higher than that obtained at 600 W. In addition, Table 5 shows the capacity comparison between $ZnCo_2O_4$ electrodes prepared in this experiment and other $ZnCo_2O_4$ electrodes.

4. Conclusion

(1) The $ZnCo_2O_4$ nanomaterials were successfully prepared via ultrasonic electrodeposition. The surface of the $ZnCo_2O_4$ anode nanomaterial prepared at 600 W exhibits a dendritic morphology with a compact structure. Furthermore, XRD results indicate that the $ZnCo_2O_4$ sample possesses a spinel structure. The $ZnCo_2O_4$ sample prepared under an ultrasonic power of 600 W displays the smallest grain size, measuring 11.68 nm.

(2) The $ZnCo_2O_4$ anode nanomaterial synthesized under an ultrasonic power of 600 W demonstrated favorable charge–discharge reversibility and stable cycling performance. Moreover, XPS results indicate the presence of zinc and cobalt oxides in the $ZnCo_2O_4$ sample.

(3) The $ZnCo_2O_4$ anode nanomaterial synthesized with a power of 600 W exhibited an optimal specific charge–discharge capacity, outstanding stability, and a high coulombic efficiency (CE) of 98.6 % following 1200 cycles at a charge–discharge process of 150 mA·g^{-1}. Furthermore, it demonstrated the lowest values of ohmic resistance (3.01 Ω) and charge transfer resistance (35.65 Ω), along with the highest diffusion coefficients of Li$^+$ among all samples, indicating superior reaction kinetics.

Declaration of competing interest

The authors declare that they have no known competing financial interests or personal relationships that could have appeared to influence the work reported in this paper.

Acknowledgments

References

Baranova, E.A., Le, P.Y., Ilin, D., 2009. Size and composition for 1–5 nm O PtRu alloy nano-particles from Cu K alpha X-ray patterns. J. Alloy. Compd. 471 (1–2), 387–394.

Etacheri, V., Marom, R., Elazari, R., Salitra, G., 2011. DAurbach, Challenges in the development of advanced Li-ion batteries: a review. Energ. Environ. Sci. 4 (9), 3243–3262.

Fu, J.X., Wong, W.T., Liu, W.R., 2015. Temperature effects on a nano-porous ZnCo$_2$O$_4$ anode with excellent capability for Li-ion batteries. RSC Adv. 93 (5), 75838–75845.

Goodenough, J.B., Park, K.S., 2013. The Li-ion rechargeable battery: a perspective. J. Am. Chem. Soc. 135 (4), 1167–1176.

Li, J., Maier, J., 2010. Rechargeable lithium batteries with aqueous electrolytes. Science 330 (6010), 1485–1488.

Liu, C., Chen, B.H., Liu, W.R., Duh, J.G., 2019. Synthesis and theoretical calculations of N-doped ZnCo$_2$O$_4$ anode for lithium-ion anode via gradient pressure-induced processes and theoretical calculations. Alloys Compd. 797 (15), 978–985.

Liu, H.W., Hu, Q.H., 2018. Novel secondary assembled micro/nano porous spheres ZnCo$_2$O$_4$ with superior electrochemical performances as lithium ion anode material. Nanotechnology 29 (32), 325603.

Liu, H., Waller, G.H., Ding, Y., Chen, D.C., Ding, D., Xi, P.X., Wang, Z.L., Liu, M.L., 2015. Controllable interior structure of ZnCo$_2$O$_4$ microspheres for high-performance lithium-ion batteries. Nano Energy 11, 64–70.

Liu, X., Wang, R.H., Liu, S.Q., Pu, J.H., Xie, H.G., Wu, M.L., Liu, D.M., Li, Y., Liu, J.W., 2023. Organic eutectic salts-assisted direct lithium regeneration for extremely low state of health Ni-rich cathodes. Adv. Energy Mater. 02987.

Lu, L., Xu, S., Lou, Z.H., Wang, S.Q., Li, G.H., Feng, C.Q., 2016. Synthesis of ZnCo$_2$O$_4$ microspheres with Zn$_{0.33}$Co$_{0.67}$CO$_3$ precursor and their electrochemical performance. J. Nanopart. Res. 18 (7), 183.

Mahmood, N., Zhang, C., Hou, Y., Liu, J., 2018. Metal oxide and hydroxide nanostructures for energy storage and conversion: synthesis, mechanisms and applications. Chem. Soc. Rev. 47 (22), 8738–8765.

Ogumi, Z., 2010. Interfacial reactions of lithium-ion batteries. Electrochemistry 78 (5), 319–324.

Qi, L., Yan, X., Sun, W., Liu, X., Meng, Y., 2020. Mesoporous Co$_3$O$_4$ microspheres as high-performance anode materials for lithium-ion batteries. Mater. Lett. 271, 127802.

Qin, X.X., Gao, J., Li, X.T., Shao, Z.C., 2017. Influence of SiO$_2$-doping on reduce graphite oxide anode material for lithium-ion battery. Russ. J. Phys. Chem. A 117 (15), 10403–10473.

Ru, Q., Song, X., Mo, Y., Guo, L., Hu, S., 2016. Carbon nanotubes modified for ZnCo$_2$O$_4$ with a novel porous polyhedral structure as anodes for lithium ion batteries with improved performances. J. Alloy. Compd. 654, 586–592.

Sahoo, S., Naik, K.K., Rout, C.S., 2015. Electrodeposition of spinel MnCo$_2$O$_4$ nanosheets for supercapacitor applications. Nanotechnology 26 (45), 455401.

Shih, G.H., Liu, W.R., 2017. A facile microwave-assisted approach to the synthesis of flower-like ZnCo$_2$O$_4$ anode materials for Li-ion batteries. RSC Adv. 67 (7), 42476–42483.

Shimizu, M., Yamanaka, R., Teranishi, T., 2021. Development of impedance measurement of lithium ion batteries electrode using terahertz chemical microscope. Electr. Eng. Jpn. 214 (4), 23355.

Sun, L., Chen, S., Wang, Y., Liu, B., Gao, X., 2019. ZnCo$_2$O$_4$ nanowires as a high-performance anode material for lithium-ion batteries. J. Power Sources 425, 101–108.

Tarascon, J.M., Armand, M., 2021. Issues and challenges facing rechargeable lithium batteries. Nature 414 (6861), 359–367.

Tiwari, N., Kadam, S., Kakade, A., Ingole, R., Kulkarni, S., 2021. Synthesis route dependent nanostructured ZnCo$_2$O$_4$ electrode material for supercapacitor application. ECS J. Solid State Sci. Technol. 10 (10), 103008.

Wang, F., Kim, S.W., Shanmukaraj, D., Wang, Z., Chen, Z., 2020. An overview of the recent progress in spherical carbon anode materials for lithium-ion batteries. J. Mater. Chem. A 8 (37), 19433–19454.

Wang, M., Qian, J., Cao, Y., Ai, X., 2019. Metal oxides/sulfides as negative electrode materials for sodium-ion batteries. Adv. Energy Mater. 9 (16), 1803460.

Wang, Z., Ru, Q., Chen, X.Q., Guo, Q., Wang, B., Hou, X.H., Hu, S.J., 2017. Solvothermal fabrication of hollow nanobarrel-like ZnCo$_2$O$_4$ towards enhancing the electrochemical performance of rechargeable lithium-ion batteries. ChemElectroChem 4 (9), 2218–2224.

Wang, L., Yang, Y., Liu, J., Li, H., Zhang, Q., Huang, X., 2018. Co$_3$O$_4$ as an advanced anode material for sodium-ion batteries. ACS Appl. Mater. Interfaces 10 (26), 22068–22075.

Wang, Y.L., Zhao, C.H., Fu, W.B., 2016. Growth of zinc cobaltate nanoparticles and nanorods on reduced graphene oxide porous networks toward high-performance supercapacitor electrodes. J. Alloy. Compd. 668, 1–7.

Wang, Z., Zhou, X., Liu, J., 2019. Metal oxide-based anodes for high-performance lithium-ion batteries. J. Mater. Chem. A 7 (6), 2543–2572.

Wei, T.T., Pang, P.P., Ji, Y.R., Zhu, Y.R., Yi, T.F., Xie, Y., 2022. Rational construction and decoration of Li$_5$Cr$_7$Ti$_6$O$_{25}$@C nanofibers as stable lithium storage materials. J. Energy Chem. 71, 400–410.

Wei, T.T., Liu, X., Yang, S.J., Wang, P.F., Yi, T.F., 2023. Regulating the electrochemical activity of Fe-Mn-Cu-based layer oxides as cathode materials for high-performance Na-ion battery. J. Energy Chem. 80, 603–613.

Winter, M., Brodd, R.J., 2004. What are batteries, fuel cells, and supercapacitors. Chem. Rev. 104 (10), 4245–4270.

Wong, W.T., Chen IV, B.H., Maggay, C.L., Duh, J.G., Liu, W.R., 2017. Synthesis and electrochemical properties of hierarchically porous Zn(Co$_{1−x}$Mn$_x$)$_2$O$_4$ anodes for li-ion batteries. Energ. Technol. 5 (9), 1526–1535.

Wu, W., Xiao, J., 2021. Graphite anode materials for lithium-ion batteries: a review of recent progress and current challenges. Adv. Energy Mater. 11 (19), 2100142.

Xu, X., Yang, Y., Zhao, Y., 2019. Advances in the preparation of modified graphite as anode materials for lithium ion batteries. J. Mater. Chem. A 7 (15), 8624–8641.

Yan, P., Zheng, J., Tang, H., Liu, J., Zhang, Y., Li, X., Liu, X., 2020. Recent advances in understanding graphite anode performance in lithium-ion batteries. Adv. Energy Mater. 10 (18), 1903550.

Yi, T.F., Qiu, L.Y., Mei, J., Qi, S.Y., Cui, P., Luo, S.H., Zhu, Y.R., Xie, Y., He, Y.B., 2020. Porous spherical NiO@NiMoO$_4$@PPy nanoarchitectures as advanced electrochemical pseudocapacitor materials. Sci. Bull. 65 (7), 546–556.

Yi, T.F., Shi, L.N., Han, X., Wang, F.F., Zhu, Y.R., Xie, Y., 2021. Approaching high-performance lithium storage materials by constructing hierarchical CoNiO$_2$@CeO$_2$ nanosheets. Energy Environ. Mater. 4, 586–595.

Yu, F., Zhang, Y., Cheng, J., Hou, Y., Liu, B., 2017. Hierarchical $ZnCo_2O_4$/Graphene composite as a high-performance anode material for lithium-ion batteries. Chem.–A Eur. J. 23 (57), 14277–14284.

Zhao, Z.J., Tian, G.Y., Trouillet, V., Zhu, L.H., Zhu, J.G., Missiul, A., Welter, E., Dsoke, S., 2019. In Operando analysis of the charge storage mechanism in a conversion $ZnCo_2O_4$ anode and the application in flexible Li-ion batteries. Inorg. Chem. Front. 6 (7), 1861–1872.

Zhou, L.F., Yang, D.R., Du, T., 2021. The current process for the recycling of spent lithium ion batteries. Front. Chem. 8, 578044.